Sr-induced dipole scatter in $Ba_xSr_{1-x}TiO_3$: Insights from a transferable-bond valence-based interatomic potential

Robert B. Wexler,[1] Yubo Qi,[2] and Andrew M. Rappe[1]

[1]*Department of Chemistry, University of Pennsylvania, Philadelphia, Pennsylvania 19104, USA*

[2]*Department of Physics and Astronomy, Rutgers University, Piscataway, New Jersey 08854, USA*

(Received 3 June 2019; revised manuscript received 12 November 2019; published 27 November 2019)

In order to design next-generation ferroelectrics, a microscopic understanding of their macroscopic properties is critical. One means to achieve an atomistic description of ferroelectric and dielectric phenomena is classical molecular dynamics simulations. Previously, we have shown that interatomic potentials based on the bond valence molecular dynamics method can be used to study structural phase transitions, ferroelectric domain nucleation, and domain wall migration in several perovskite oxides and fixed-composition binary and ternary alloys. Most modern devices, however, use variable-composition perovskite oxide alloys such as $Ba_xSr_{1-x}TiO_3$ (BST). In this paper, we extend our bond valence approach to BST solid solutions and, in so doing, show that the potential parameters for each element are transferable between materials with different x. Using this potential, we perform bond valence molecular dynamics simulations investigating the temperature and composition dependence of the lattice constants, Ti displacements, and ferroelectric polarization of BST and find that our predictions match experiments and first-principles theory. Additionally, based on a detailed analysis of local dipole distributions in rhombohedral BST, we demonstrate that substitution of Sr for Ba scrambles dipoles, reduces global polarization, and enhances the order-disorder character of the ferroelectric-paraelectric phase transition.

DOI: 10.1103/PhysRevB.100.174109

I. INTRODUCTION

$Ba_xSr_{1-x}TiO_3$ (BST) is a special family of dielectric/ferroelectric alloy perovskites that feature high dielectric constant, low dielectric loss, and highly nonlinear dielectric response. This unique combination of physical properties lends BST to applications such as tunable microwave devices (e.g., phase shifters, tunable filters, resonators, and delay lines), capacitors for dynamic random-access memory, piezoelectric actuators for radio-frequency microelectromechanical systems, varicap diodes for telecommunications (e.g., voltage-controlled oscillators), and IR, humidity, and gas microsensors [1–19]. In addition to its favorable dielectric properties, BST offers highly tunable ferroelectric properties due to its three structural phase transitions as a function of temperature and composition x. For example, the Curie temperature T_C of BST decreases by 265 K from 391 to 126 K as x decreases from 1 ($BaTiO_3$) to 0.12 ($Ba_{0.12}Sr_{0.88}TiO_3$) [6–10]. Currently, however, there is a great need to understand the dielectric/ferroelectric dynamics for the whole composition range of BST in order to inform the design of next-generation materials for the aforementioned applications.

Bond valence-based interatomic potentials have proven to be a powerful tool, enabling fast and large-scale molecular dynamics simulations of ferroelectric oxides. Interatomic potentials for several technologically important perovskite materials, such as $BaTiO_3$, $PbTiO_3$, $PbZrO_3$, and $BiFeO_3$, have been successfully developed [20–25]. In addition, bond valence molecular dynamics potentials successfully describe $Pb(Zr_{0.5}Ti_{0.5})O_3$ (PZT) and $Pb(Mg_{0.25}Ti_{0.25}Nb_{0.5})O_3$-$PbTiO_3$ (25% PMN-PT), single-composition binary and ternary alloys [20–30]. In these potentials, however, the parameters corresponding to a specific element are material dependent, not just species dependent. For example, the fitted Coulombic charges for oxygen are different in each material, which makes bond valence molecular dynamics simulations for arbitrary x of $(A_xA'_{1-x})BO_3$ or $A(B_xB'_{1-x})O_3$ alloys impossible. Given this limitation, we aim to develop transferable interatomic potentials where the parameters corresponding to a particular element depend only on that element's intrinsic properties and therefore can be used for different materials and their heterostructures and alloys with diverse chemical compositions. In this paper, we report the successful development of a transferable interatomic potential for BST. Bond valence molecular dynamics simulations using this potential accurately reproduce the experimentally determined temperature-composition phase diagram of BST. Additionally, the atomistic nature of our interatomic potential enables analysis of local dipole distributions, which reveal that the substitution of Sr for Ba weakens the correlation between and promotes arbitrarily oriented Ti displacements, suppresses the global polarization, and changes the character of the ferroelectric-paraelectric phase transition. This work not only presents proof of concept for the development of element-dependent, transferable-bond valence molecular dynamics interatomic potentials but also provides atomistic insights into the relationship between the thermodynamic properties of BST and its composition.

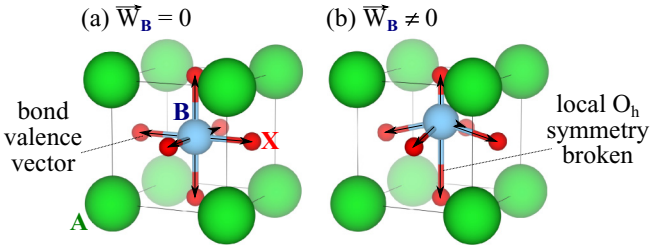

FIG. 1. (a) A centrosymmetric perovskite structure with zero bond valence vector sum and (b) a polar perovskite structure with nonzero bond valence vector sum. The Ba, Ti, and O atoms are represented by green, blue, and red spheres, respectively.

II. COMPUTATIONAL METHODS

A. Bond valence-based interatomic potentials

In the bond valence model, the valence of a bond V_{ij} between atoms i and j is defined as the number of electron pairs used to form that bond and is expressed mathematically as

$$V_{ij} = \left(\frac{r_{0,ij}}{r_{ij}}\right)^{C_{ij}}, \tag{1}$$

where $r_{0,ij}$ is a reference distance between atoms i and j, r_{ij} is the instantaneous distance, and C_{ij} is an empirical parameter related to the force constant of the chemical bond [21,23–26,31–34]. The valence of atom i (V_i) is obtained by summing the bond valences of the bonds it forms with its neighbors j,

$$V_i = \sum_j^{N_n} V_{ij}, \tag{2}$$

where N_n is the number of neighbors. Due to the bond valence conservation principle, there is an energy penalty E_{BV} if the atomic valence deviates from its optimal value $V_{0,i}$,

$$E_{\mathrm{BV}} = \sum_i^{N_a} S_i\left(V_i - V_{0,i}\right)^2, \tag{3}$$

where N_a is the number of atoms in the unit cell and S_i is a scaling factor. Chemically speaking, E_{BV} describes the energy increase associated with over- and undercoordination of atoms.

The bond valence vector is defined as $\vec{V}_{ij} = V_{ij}\hat{R}_{ij}$, where $\hat{R}_{ij}$ is the unit vector pointing from atom i to atom j. The sum of the bond valence vectors of atom i

$$\vec{W}_i = \sum_j^{N_n} \vec{V}_{ij} \tag{4}$$

is a measure of local symmetry breaking. Take, for example, the perovskite ABX_3 structure shown in Fig. 1. In Fig. 1(a), the B-site cation sits at the center of an octahedral cage of X anions. In this arrangement, the B-X bond valence vectors cancel, yielding a zero bond valence vector sum for the B-site cation. If the B-site cation displaces off center, as in Fig. 1(b), the bond valence vectors along the displacement direction no longer cancel, leading to a nonzero bond valence vector sum for the B-site cation. Similar to Eq. (3), a bond valence vector

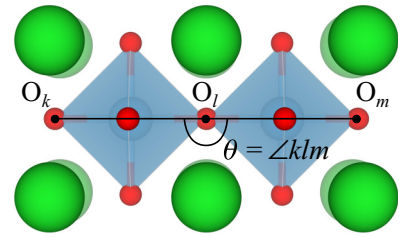

FIG. 2. Schematic representation of the angle potential.

energy E_{BVV} can be written as

$$E_{\mathrm{BVV}} = \sum_i^{N_a} D_i\left(\vec{W}_i^2 - \vec{W}_{0,i}^2\right)^2, \tag{5}$$

where D_i is a scaling factor and $|\vec{W}_{0,i}|$ is the preferred bond valence vector length. This energy term is important for capturing the equilibrium off-center displacements of ions ($\vec{W}_{0,i} \neq 0$) in ferroelectric materials. Previously, we showed that E_{BV} and E_{BVV} are equivalent to second- and fourth-moment bond order potentials, respectively [35]. This equivalence shows that Eqs. (3) and (5) have a quantum-mechanical foundation [23,24,34,36,37].

In our scheme, the total energy of the system is given by

$$E = E_{\mathrm{BV}} + E_{\mathrm{BVV}} + E_r + E_c + E_a, \tag{6}$$

$$E_r = \sum_{i<j}\left(\frac{B_{ij}}{r_{ij}}\right)^{12}, \tag{7}$$

$$E_c = \sum_{i<j}\frac{q_i q_j}{r_{ij}}, \tag{8}$$

$$E_a = k\sum_i (\theta_i - 180^\circ)^2, \tag{9}$$

where E_r is the short-range repulsion energy, E_c is the Coulomb energy, E_a is the X_6 octahedral tilting energy, B_{ij} is the short-range repulsion parameter, q is the charge in units of $|e|$, k is a scaling factor, and θ_i is the octahedral tilting angle (see Fig. 2) in degrees calculated as $\angle klm$.

Bond valence-based interatomic potentials enable efficient, large-scale molecular dynamics simulations and have been used successfully in the past to study structural phase transitions [20–25], the nucleation of ferroelectric domains [38–40], the dynamics of the walls separating these domains in perovskites [39], and relaxor ferroelectrics [27–30]. For this reason, we have developed interatomic potentials for several technologically important perovskites such as $PbTiO_3$ [20–22,24,40], $BiFeO_3$ [23,41,42], $PbZrO_3$, $BaTiO_3$ (BTO) [25], PZT [20,26], and PMN-PT [27–30]. Based on these successes, we extend this approach to include the perovskite alloy family BST. We note that our previously developed interatomic potential for BTO accurately reproduces many physical properties such as lattice constants, permittivities, and the structural phase transition sequence. Therefore, the parameters related to Ba, Ti, and O elements are kept fixed, and only those related to Sr ($r_{0,\mathrm{SrO}}$, C_{SrO}, S_{Sr}, D_{Sr}, and $B_{\mathrm{Sr}X}$, where $X \in \{\mathrm{Ba, Sr, Ti, O}\}$) were optimized. Additionally, in order to maintain charge neutrality, we set the charge of Sr equal to that of Ba.

TABLE I. Optimized parameters of the bond valence-based interatomic potential for BST. The scaling constant k is 0.0609 eV/(deg)^2.

						$B_{\beta\beta'}$ (Å)					
	$r_{0,\beta O}$	$C_{0,\beta O}$	q_β (e)	S_β (eV)	D_β	Ba	Sr	Ti	O	$V_{0,\beta}$	$\vec{W}_{0,\beta}$
Ba	2.290	8.94	1.34730	0.59739	0.08429	2.44805	2.40435	2.32592	1.98792	2.0	0.11561
Sr	2.143	8.94	1.34730	0.63624	9.99121		0.38947	1.68014	1.96311	2.0	0.00000
Ti	1.798	5.20	1.28905	0.16533	0.82484			2.73825	1.37741	4.0	0.39437
O			−0.87878	0.93063	0.28006				1.99269	2.0	0.31651

B. Parameterization

The parameters of the interatomic potential were fit to reproduce density functional theory (DFT) [43,44] calculations of BST using the optimization protocol described in the Supplemental Material [45] (see Fig. S1, its accompanying text, and also Refs. [46–48] therein). DFT calculations were carried out using the QUANTUM ESPRESSO software package [49]. Designed [50], optimized, norm-conserving pseudopotentials [51] were used to replace the core electrons with a smoother, effective potential. The exchange-correlation contribution to the total energy was calculated using the revised Perdew-Burke-Ernzerhof generalized gradient approximation for solids (PBEsol), which provides excellent agreement with the experimental lattice parameters and spontaneous polarization of BTO [52]. The electronic wave functions were expanded in a plane-wave basis set with an energy cutoff of 60 Ry. Integrals over the Brillouin zone were evaluated using a Γ-centered, $4 \times 4 \times 4$ k-point mesh. Our database consists of 612 structures extracted from variable-cell relaxations; every structure is a $2 \times 2 \times 2$ supercell containing 40 atoms. The total energy, force, and pressure convergence criteria for these relaxations were 1.4×10^{-5} eV/supercell, 2.7×10^{-4} eV/Å, and 0.5 kbar, respectively. For self-consistent field calculations, the total energy convergence threshold was 1.4×10^{-8} eV/supercell. The average absolute difference between the DFT and molecular dynamics energies is 1.12×10^{-3} eV/atom. The optimized parameters are listed in Table I.

C. Molecular dynamics simulations

Molecular dynamics simulations were performed using an in-house version of the Large-scale Atomic Molecular Massively Parallel Simulator (LAMMPS) [53] that was modified to calculate the bond valence and bond valence vector energies. We investigated five different concentrations of Sr in BST: 10%, 30%, 50%, 70%, and 90%. For each concentration, Ba was replaced with Sr randomly. Every structure is a $20 \times 20 \times 20$ supercell containing 40 000 atoms. We find this to be more than sufficient (only $10 \times 10 \times 10$ is necessary) to converge the structural phase transition sequence of $Ba_{0.9}Sr_{0.1}TiO_3$ (see Fig. S2 in the Supplemental Material). Long-range Coulombic interactions were computed using the particle-particle particle-mesh solver with a desired absolute error in the forces of 1×10^{-4} eV/Å. The cutoff distance for short-range interactions was chosen to be 8 Å. Neighbor lists, containing all atom pairs within 10 Å, were updated every step. The time step for molecular dynamics simulations was 1 fs. We studied temperatures ranging from 10 to 170 K. For each temperature, the simulation consisted of three steps: (1) NVT equilibration, (2) NPT equilibration, and (3) NPT sampling. The first step runs for 10 ps and generates positions and velocities sampled from the canonical ensemble using the Nosé-Hoover thermostat [54–56] with a temperature-damping parameter of 1 ps. The second step relaxes the volume constraint to sample from the isothermal-isobaric ensemble for 40 ps at 1.01325 bars using the Parrinello-Rahman barostat [57,58] with a pressure-damping parameter of 5 ps. The third step samples the NPT-equilibrated structure for 40 ps, from which thermodynamic time averages can be computed.

III. RESULTS AND DISCUSSION

A. Thermodynamic properties of BST

We tested the performance of the interatomic potential for BST by calculating the lattice constants, components of the Ti displacements, and components of the polarization as a function of the temperature and concentration of Sr. Figure 3(a) shows how the lattice constants change as BST is heated from low to high temperature. For 10% Sr, the evolution of the lattice constants is very similar to that of BTO. It is well known experimentally that BTO undergoes three structural phase transitions: (1) from rhombohedral ($P \parallel [111]$) to orthorhombic ($P \parallel [110]$), (2) from orthorhombic to tetragonal ($P \parallel [100]$), and (3) from tetragonal to cubic ($P = 0$) [59–61]. First, we will discuss BST with 10% Sr. At temperatures less than or equal to 90 K, a rhombohedral phase is preferred. Between 90 and 110 K, BST becomes orthorhombic. From 110 to 140 K, the system favors a tetragonal crystal structure. Finally, at 140 K, a tetragonal to cubic phase transition occurs. The rhombohedral to orthorhombic to tetragonal to cubic phase transition sequence is in excellent qualitative agreement with experiments and other computational studies [59–64]. The phase transition temperatures, however, are systematically underestimated, as has been shown for other theoretical models based on DFT [23,62–69]. These underestimations are attributed primarily to systematic errors in DFT exchange-correlation functionals. Improvements in the phase transition temperatures can be made by using *ad hoc* correction schemes such as scaling the DFT potential energy surface [68] and applying negative pressures [66,69]. With that being said, we do not use such schemes so as to avoid semiempirical extrapolation, which may lead to unphysical dynamics. As the concentration of Sr is increased, the rhombohedral-orthorhombic and tetragonal-cubic phase transition temperatures decrease, and the orthorhombic and tetragonal phases disappear at and above 70% Sr, both of which are seen experimentally [59–61]. Additionally, we find that the lattice constants of BST

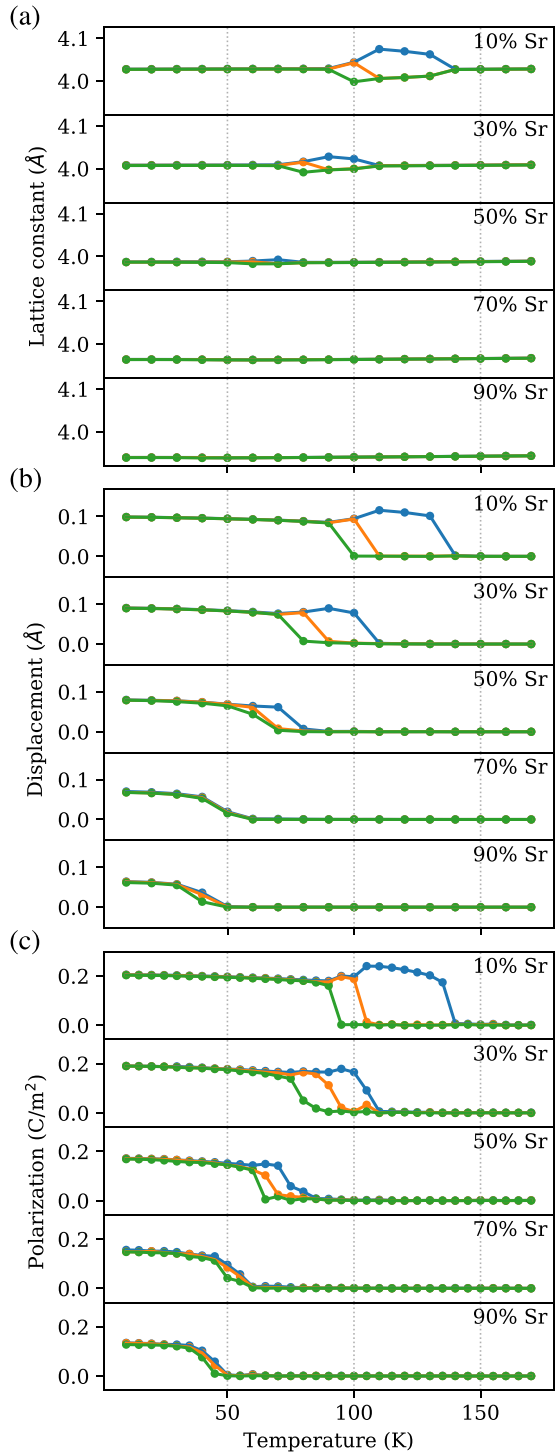

FIG. 3. Temperature dependence of the (a) lattice constants, (b) Ti displacements, and (c) polarization components of BST for different compositions.

decrease with increasing Sr content because the ionic radius of Sr (1.44 Å) is smaller than that of Ba (1.61 Å).

In addition to the crystal lattice, the position of Ti relative to the center of its O_6 octahedral cage also depends on the temperature and composition of BST, as shown in Fig. 3(b). There are four possible displacement modes of Ti: [111], [110], [100], and [000], where the last corresponds to Ti at the center of the octahedron. The transition temperatures for the Ti displacements are the same as those for the structural phase transitions, so they will not be repeated here. For 10% and 30% Sr, three different displacement transitions are observed: (1) from [111] to [110], (2) from [110] to [100], and (3) from [100] to [000], ranked from the lowest to highest transition temperature. This ordering is the same as that of BTO and is consistent with experimental measurements of the Ti displacement [60]. The magnitude of the Ti displacement decreases as more Sr is introduced into the system because the shrinking of the lattice reduces the room for Ti to move off center.

We also analyzed the effect of temperature and Sr concentration on the polarization of BST. The polarization plotted in Fig. 3(c) is calculated as

$$\vec{P}(t) = \frac{1}{N_u}\sum_{i}^{N_u}\vec{P}_i(t), \tag{10}$$

where t is time, N_u is the number of unit cells, and P_i is the polarization of unit cell i,

$$\vec{P}_i(t) = \frac{1}{\Omega_i}\left(\frac{1}{8}\sum_{j=1}^{8}\mathbf{Z}_A^*\vec{r}_{A,j}(t) + \mathbf{Z}_{\mathrm{Ti}}^*\vec{r}_{\mathrm{Ti}}(t) + \frac{1}{2}\mathbf{Z}_{\mathrm{O}}^*\cdot\sum_{j=1}^{6}\vec{r}_{\mathrm{O},j}(t)\right), \tag{11}$$

where Ω is the volume of the unit cell, $\mathbf{Z}^*$ are the Born effective charge tensors (taken from Ref. [70]), A is either Ba or Sr, and $\vec{r}$ is the position of each atom relative to the center of the unit cell. Here, we define a unit cell as having eight A-site cations at the corners, one Ti at the center, and six O at the face centers. The temperature profile of the polarization components is very similar to that of the Ti displacements. For Sr concentrations less than 30%, the direction of the polarization changes from [111] to [110] to [100] to [000]. The last change is a ferroelectric to paraelectric phase transition that occurs at T_C. Increasing the amount of Sr reduces the T_C substantially, which is in excellent agreement with the experimental literature on BST [59–61]. The magnitude of the [111] polarization for 10% Sr (0.35 $\mathrm{C/m^2}$) also matches previous experimental (0.31 $\mathrm{C/m^2}$) [60] and computational (0.16 and 0.44 $\mathrm{C/m^2}$) [62,64] reports.

We would like to note that our interatomic potential predicts both $BaTiO_3$ and $SrTi_3$ have no octahedral tilting. While this is true for $BaTiO_3$, $SrTiO_3$ should have a small, but nonzero, octahedral tilting, as evidenced by experiments [71] and other DFT calculations using PBEsol [69,72]. This does not appear to affect our results as octahedral rotations are on a smaller energy scale and the lattice constants, ferroelectric displacements, and structural phase transitions are all well described.

B. Temperature-composition phase diagram

As a next step in validating our interatomic potential, we construct the temperature-composition phase diagram of BST and compare it with experiments. The phase diagram is shown in Fig. 4, where the rhombohedral, orthorhombic, tetragonal, and cubic phases are shaded red, orange, blue, and green, respectively. We are able to reproduce two key features of the phase diagram: (1) the shifts of the ferroelectric-paraelectric

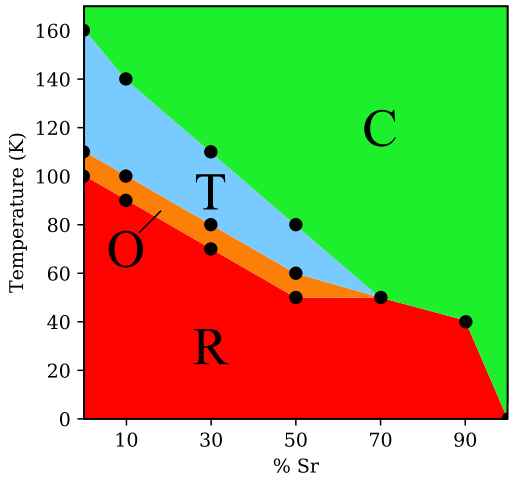

FIG. 4. Temperature-composition phase diagram of BST. Black circles correspond to the results of our simulations. Red, orange, blue, and green correspond to the extrapolated regions where the rhombohedral, orthorhombic, tetragonal, and cubic phases are stable, respectively.

and ferroelectric-ferroelectric phase transition lines to lower temperature with increasing Sr concentration and (2) the presence of a tricritical point near 70% Sr. It has been shown that, at the tricritical point, the character of the ferroelectric-paraelectric phase transition goes from first order to second order [59,61]. This can been seen in Fig. 3(c), where, between 50% Sr and 70% Sr, the transition from nonzero to zero polarization becomes less sharp. This can also be seen in Figs. S5–S8 (see Sec. S3 of the Supplemental Material), which plot the temperature and composition dependence of the total energy at 1.01325 bars. For 10% Sr, latent heats are observed (see Figs. S5–S7), which indicates a series of first-order phase transitions with increasing temperature. At 90% Sr, however, there is no latent heat (see Fig. S8), thus revealing a change in the order of the phase transition from first to second.

C. Effects of Sr substitution on dipolar structure

The strong agreement between bond valence molecular dynamics and experimental phase diagrams indicates that this bond valence molecular dynamics interatomic potential for BST is accurate and can be used to explore the atomistic origins of structural phase transitions in solid solutions.

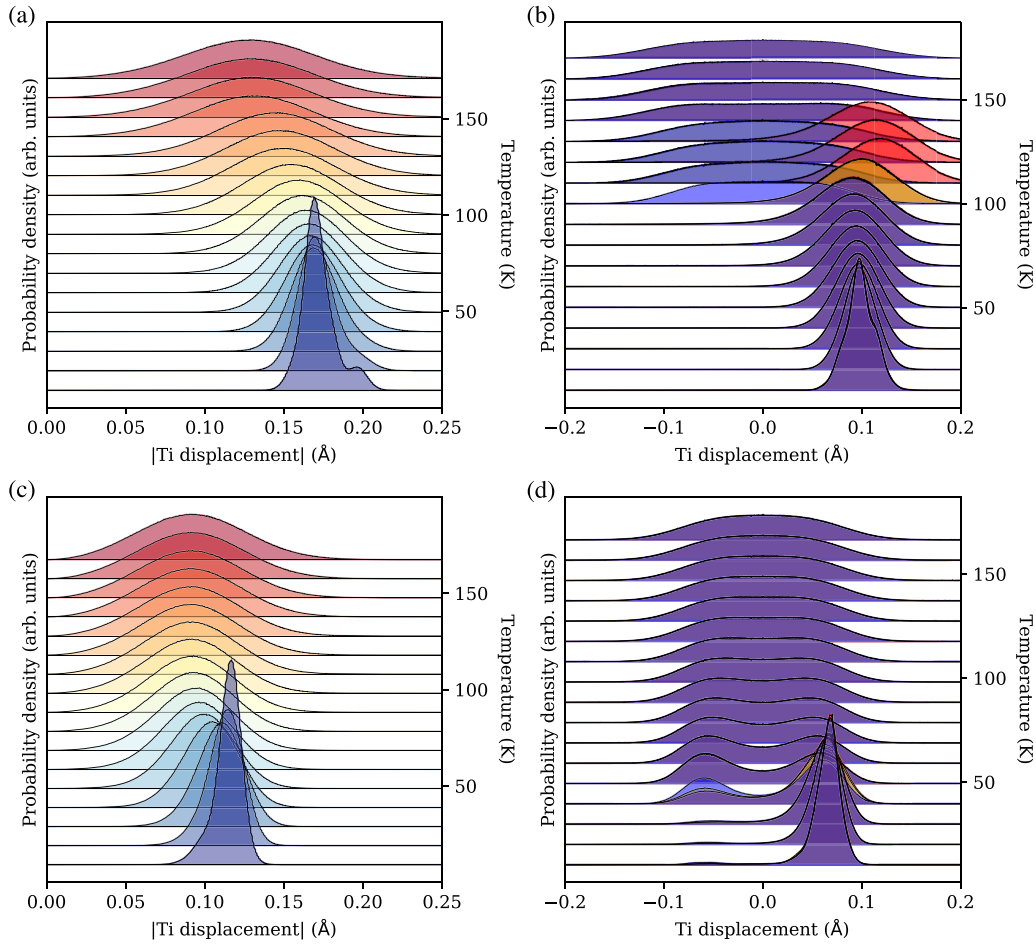

FIG. 5. Temperature dependence of (a) $|d_{Ti}|$ distributions and (b) Ti displacement distributions in three Cartesian directions for $Ba_{0.9}Sr_{0.1}TiO_3$. Those for $Ba_{0.1}Sr_{0.9}TiO_3$ are shown in (c) and (d), respectively. The colors in (a) and (c) correspond to the temperature of the simulation, with blue being the coldest (10 K) and red being the hottest (170 K). The colors in (b) and (d) correspond to the components of the Ti displacement in the three Cartesian directions: x is red, y is yellow, and z is blue. If some or all of these distributions overlap, then the resulting color is additive, e.g., red + yellow = orange. Note that the temperature in (a)–(d) is also given by the secondary y axis.

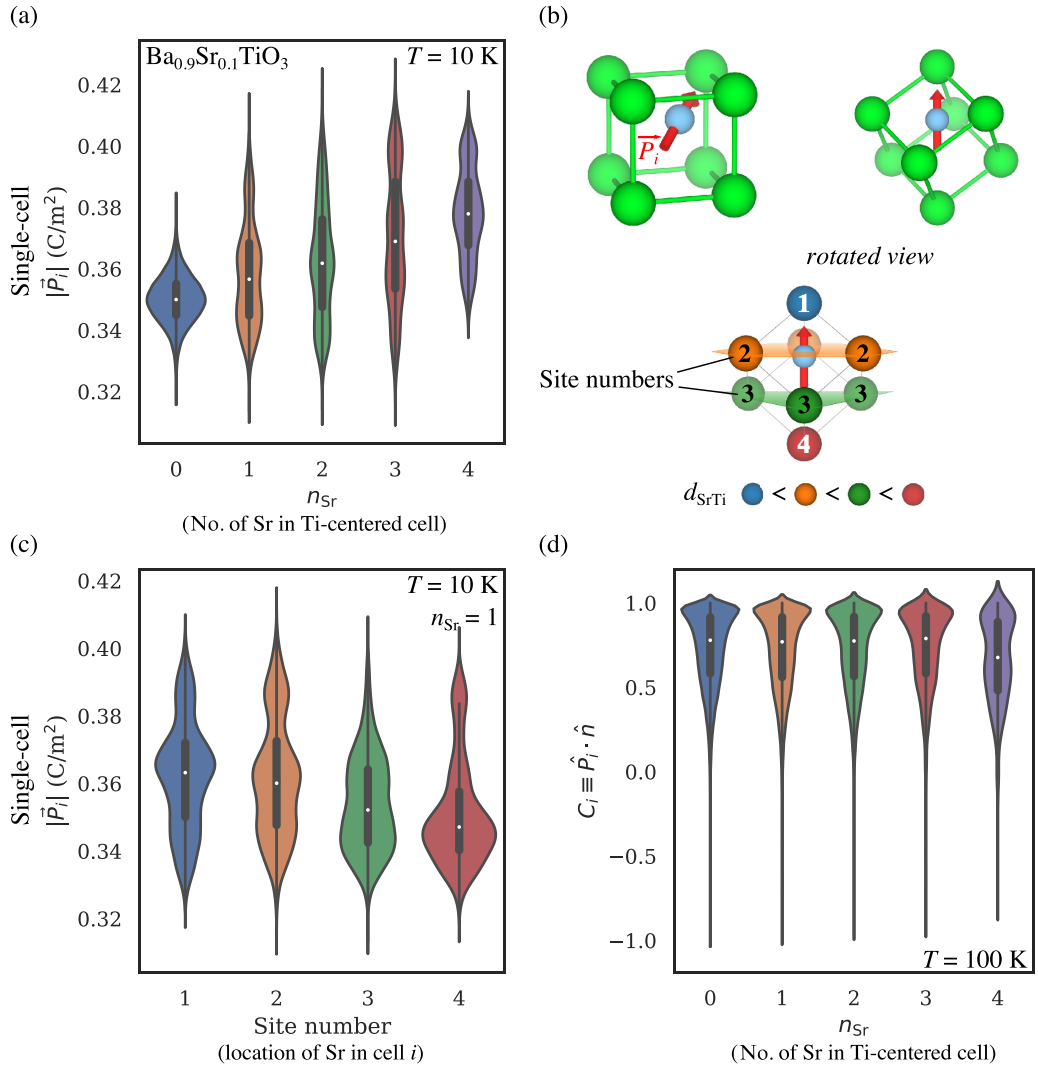

FIG. 6. The role of Sr dopants enhancing low-T polarization in $Ba_{0.9}Sr_{0.1}TiO_3$. (a) Dependence of the single-cell polarization magnitude $|\vec{P}_i|$ on n_{Sr} at 10 K. We use a kernel density estimation of the underlying distribution. The bottom and top of the black rectangle correspond to the first and third quartiles, respectively. White points correspond to the median single-cell polarization magnitude. (b) The top shows the eight nearest-neighbor A sites. The bottom shows the four unique A sites for [111] polarized Ti. (c) Dependence of the single-cell polarization magnitude on the site number of the A site occupied by Sr for $n_{Sr} = 1$. Numbering corresponds to the bottom of (b). (d) Dependence of the orientational correlation between dipoles, calculated as $C_i \equiv \hat{P}_i \hat{n}$, on the number of local Sr at 100 K.

In order to investigate changes in local physicochemical properties with Sr substitution, we examine the temperature dependence of the Ti displacement distributions of Ba-rich BST [$Ba_{0.9}Sr_{0.1}TiO_3$; see Figs. 5(a) and 5(b)] and Sr-rich BST [$Ba_{0.1}Sr_{0.9}TiO_3$; see Figs. 5(c) and 5(d)]. Figure 5(a) shows that, for Ba-rich BST, the absolute values of the Ti displacements $|d_{Ti}|$ are normally distributed at all temperatures except at 10 K, where two peaks are observed. The larger peak at 0.17 Å corresponds to the displacement of Ti atoms that are completely surrounded by Ba at the A sites. The smaller peak at 0.20 Å, however, originates from Ti atoms whose neighboring A sites are partially occupied by Sr [62]. The effect of Sr on $|d_{Ti}|$ can be seen more clearly in Fig. 6(a), where the distribution of the single-cell polarization magnitude is plotted against the number of Sr in a Ti-centered cell n_{Sr}. Each Ti has eight nearest-neighbor A sites, and each of these can host either Ba or Sr. Consequently, we define n_{Sr} as the number of Sr occupying nearest-neighbor A sites for a particular Ti. We find that as n_{Sr} increases from 0 to 4, the median single-cell polarization magnitude [shown as white points in Fig. 6(a)] increases from 0.350 to 0.378 C/m^2. The reason for the increased Ti displacement near Sr is that, for low Sr doping concentrations, the lattice constant does not change, but Sr takes up less volume than Ba. Therefore, the free volume available for off-center Ti displacements is larger when Sr is adjacent. The magnitude of this effect also depends on the position of Sr relative to that of Ti. If Ti is polarized along [111], then there are four unique A sites [see Fig. 6(b)]. Figure 6(c) shows that, for $n_{Sr} = 1$, as the distance between Sr and Ti increases, the median single-cell polarization magnitude decreases from 0.363 to 0.347 C/m^2. This suggests that the free volume created by replacing Ba with Sr is more accessible to Ti and subsequently more effective at increasing its polarization when Sr and Ti are closer. Additionally, the

multipeak structure for $n_{Sr} \geqslant 1$ in Fig. 6(a) can be rationalized by the fact that, for different Sr-Ti distances, the single-cell polarization magnitude distribution is centered at different values. It can also be seen in Fig. 5(a) that Ti shifts to smaller displacements with a broader distribution at higher temperatures. The decrease in the mean displacement vs temperature is consistent with the Landau-Ginzburg-Devonshire theory of first-order ferroelectric-paraelectric phase transitions [73–75]. The structural phase transitions of BST also contribute to this decrease by suppressing components of the displacement. On the other hand, the increase in the standard deviation of the Ti displacement magnitude is due to thermal randomization in the presence of disorder. Despite the mean decrease, the distribution remains centered at nonzero displacements even in the paraelectric phase. This suggests that the ferroelectric-paraelectric phase transition of Ba-rich BST has order-disorder character.

The individual phase transitions of Ba-rich BST can be seen more clearly in Fig. 5(b), which plots the distribution of the Ti displacement components against temperature. The x, y, and z components are shaded red, yellow, and blue, respectively. For temperatures below 100 K, the three distributions are superimposed, resulting in a single Gaussian (shaded purple). At 100 K, there is a rhombohedral to orthorhombic phase transition that zeros the mean and flattens the distribution of the z component (shaded blue). The same thing happens to the remaining nonzero components at the higher-temperature phase transitions, i.e., orthorhombic-tetragonal at 110 K and tetragonal-cubic (ferroelectric-paraelectric) at 130 K. This plateauing of the distribution is characteristic of simultaneously order-disorder and displacive phase transitions [25]. Therefore, the phase transitions of Ba-rich BST exhibit mixed order-disorder and displacive character, which is quite similar to pure BTO [25,76,77].

The distribution of the Ti displacement magnitude for Sr-rich BST is plotted in Fig. 5(c). At low temperatures (10 K), the peak of the distribution is located at 0.12 Å, which is smaller than those for Ba-rich BST (0.17 and 0.20 Å). For Sr-rich BST, the lattice constant is primarily determined by the ionic radius of Sr, which is smaller than that of Ba; this decrease in the lattice constant leads to a reduction in free volume and a suppression of the Ti displacements. The distribution of the Ti displacement components vs temperature [see Fig. 5(d)] shows a change in the character of the ferroelectric-paraelectric phase transition that is due to the high concentration of Sr. At low temperatures (10 K), nearly all of the Ti displacements are directed along [111] (shaded purple). There are some antiparallel displacements, however, as indicated by the small peak at −0.06 Å, which suggests that the orientational correlation between dipoles is weakened by the presence of Sr. As the temperature increases (20 K $< T <$ 40 K), the height of the antiparallel peak increases, revealing that the character of the ferroelectric-paraelectric phase transition is predominantly order-disorder. We should also emphasize that, at 40 K, unit cells resembling all three polar phases [rhombohedral (shaded purple), orthorhombic (shaded orange), and tetragonal (shaded blue)] coexist, but due to the lack of strong correlation between dipoles, no single polar phase dominates. At 50 K, the two peaks have equal height, revealing an order-disorder nonpolar state. As the temperature increases further ($T >$ 50 K), the value of the distribution at zero displacement begins to rise, indicating the appearance of displacive character in the phase transition.

In order to analyze the effect of n_{Sr} on the orientation correlation of Ti dipoles, we return to the case of Ba-rich BST, as it allows us to quantify the effect of individual Sr^{2+} cations. Here, we define the orientational correlation of the Ti dipole as

$$C_i \equiv \hat{P}_i \cdot \hat{n}, \tag{12}$$

where $\hat{P}_i$ is the local polarization direction and $\hat{n}$ is the [111] direction. Figure 6(d) shows that as n_{Sr} is increased from 0 to 4, the median orientational correlation between dipoles decreases from 0.726 to 0.659 at 100 K, i.e., the rhombohedral-orthorhombic phase transition temperature. Consistent with the decrease in the median orientational correlation between dipoles, the distribution also shows more dipoles far from [111]. These features suggest that Sr weakens Ti dipole correlations. The extent of the reduction of the orientational correlation between dipoles depends monotonically on n_{Sr}. For all n_{Sr}, there are a few Ti that are antiparallel to [111], as indicated by the thin, but nonzero, distributions at negative orientational correlations between dipoles. These Ti have undergone thermally induced, local polarization switching due to the rhombohedral-orthorhombic phase transition. Analysis of the orientational correlation between dipoles enriches our view of the dipolar structure and influence of Sr on Ti by providing quantitative insights about the role of Sr doping in dipole scattering; we observe antiparallel-oriented dipoles for all numbers of local Sr and a significant weakening of the dipole correlation for $n_{Sr} > 3$.

IV. CONCLUSIONS

In conclusion, we have developed a robust interatomic potential for BST based on the bond valence method. This potential enables accurate and efficient large-scale molecular dynamics simulations of ferroelectric alloy phenomena at the atomistic level. Here, we examined the temperature and composition dependence of the lattice parameters, Ti displacements, and polarization and achieved excellent correspondence with experiment. Additionally, our BST potential is transferable in the sense that the parameters for each element are taken from potentials for other materials that contain the same elements, namely, BTO and STO. Such transferability facilitates the construction of potentials for complex perovskite alloy families. Due to the atomistic nature of this potential, we are able to investigate the temperature dependence of the local dipole distributions for both Ba-rich and Sr-rich BST. We discover that the ferroelectric-paraelectric phase transition character of BTO does not change significantly upon 10% Sr doping. However, in Sr-rich BST, the character of the phase transition is order-disorder at low temperatures due to the Sr-induced weakening of dipole correlations, with displacive character emerging only at higher temperatures. Looking forward, alloy bond valence molecular dynamics potentials enable not only the prediction of macroscopic (lattice constants, polarization, structure phase transitions, and their temperatures) and microscopic (Ti displacements) physical properties of technologically important ferroelectric perovskite alloys such as BST, BZT, PZT, and PMN-PT but

also the nanoscale design of new materials via compositional tuning and heterostructure/superlattice engineering [78–94].

ACKNOWLEDGMENTS

R.B.W. and Y.Q. acknowledge support from the US Office of Naval Research, under Grant No. N00014-17-1-2574. A.M.R. acknowledges support from the DOE Office of Basic Energy Sciences, under Grant No. DE-FG02-07ER46431. The authors also acknowledge computational support from the High-Performance Computing Modernization Office and the National Energy Research Scientific Computing Center.

[1] S. Oh, J.-H. Park, and J. Akedo, IEEE Trans. Ultrason. Ferroelectr. Freq. Control **56**, 421 (2009).
[2] C. S. Hwang, S. O. Park, H.-J. Cho, C. S. Kang, H.-K. Kang, S. I. Lee, and M. Y. Lee, Appl. Phys. Lett. **67**, 2819 (1995).
[3] D. O'Neill, G. Catalan, F. Porras, R. Bowman, and J. Gregg, J. Mater. Sci.: Mater. Electron. **9**, 199 (1998).
[4] C. Chen, H. Feng, Z. Zhang, A. Brazdeikis, Z. Huang, W. Chu, C. Chu, F. Miranda, F. Van Keuls, R. Romanofsky *et al.*, Appl. Phys. Lett. **75**, 412 (1999).
[5] P. Joshi and M. Cole, Appl. Phys. Lett. **77**, 289 (2000).
[6] Y. Teh, N. Ong, Z. Sauli, J. Alcain, and V. Retnasamy, in *Third Electronic and Green Materials International Conference 2017 (EGM 2017)*, AIP Conf. Proc. No. 1885 (AIP, New York, 2017), p. 020290.
[7] M. R. Mohammadi and D. J. Fray, Particuology **9**, 235 (2011).
[8] Y. Bian and J. Zhai, J. Phys. Chem. Solids **75**, 759 (2014).
[9] S. H. Xiao, W. F. Jiang, K. Luo, J. H. Xia, and L. Zhang, Mater. Chem. Phys. **127**, 420 (2011).
[10] D. Tahan, A. Safari, and L. Klein, in *Proceedings of 1994 IEEE International Symposium on Applications of Ferroelectrics* (IEEE, New York, 1994), pp. 427–430.
[11] X. Chen, Y. Tian, H. Liu, C. Du, J. Li, and P. Yu, Ceram. Int. **39**, S517 (2013).
[12] S. Fuentes, E. Chávez, L. Padilla-Campos, and D. Diaz-Droguett, Ceram. Int. **39**, 8823 (2013).
[13] H. Chen, C. Yang, B. Wang, H. Ji, and J. Zhang, J. Appl. Phys. **105**, 034112 (2009).
[14] H.-S. Kim, T.-S. Hyun, H.-G. Kim, I.-D. Kim, T.-S. Yun, and J.-C. Lee, Appl. Phys. Lett. **89**, 052902 (2006).
[15] C. Fu, F. Pan, H. Chen, S. Feng, W. Cai, and C. Yang, J. Infrared Millimeter Terahertz Waves **28**, 229 (2007).
[16] T. Yamada, V. O. Sherman, A. Nöth, P. Muralt, A. K. Tagantsev, and N. Setter, Appl. Phys. Lett. **89**, 032905 (2006).
[17] C. Chen, J. Shen, S. Chen, G. Luo, C. Chu, F. Miranda, F. Van Keuls, J. Jiang, E. Meletis, and H. Chang, Appl. Phys. Lett. **78**, 652 (2001).
[18] W. Zhu, O. Tan, J. Deng, and J. Oh, J. Mater. Res. **15**, 1291 (2000).
[19] O. Tan, X. Chen, and W. Zhu, Ferroelectrics **225**, 295 (1999).
[20] V. R. Cooper, I. Grinberg, and A. M. Rappe, in *Fundamental Physics of Ferroelectrics 2003*, AIP Conf. Proc. No. 677 (AIP, New York, 2003), p. 220.
[21] Y.-H. Shin, V. R. Cooper, I. Grinberg, and A. M. Rappe, Phys. Rev. B **71**, 054104 (2005).
[22] Y.-H. Shin, B.-J. Lee, and A. M. Rappe, J. Korean Phys. Soc. **52**, 1206 (2008).
[23] S. Liu, I. Grinberg, and A. M. Rappe, J. Phys.: Condens. Matter **25**, 102202 (2013).
[24] S. Liu, I. Grinberg, H. Takenaka, and A. M. Rappe, Phys. Rev. B **88**, 104102 (2013).
[25] Y. Qi, S. Liu, I. Grinberg, and A. M. Rappe, Phys. Rev. B **94**, 134308 (2016).
[26] I. Grinberg, V. R. Cooper, and A. M. Rappe, Nature (London) **419**, 909 (2002).
[27] H. Takenaka, I. Grinberg, and A. M. Rappe, Phys. Rev. Lett. **110**, 147602 (2013).
[28] H. Takenaka, I. Grinberg, S. Liu, and A. M. Rappe, Nature (London) **546**, 391 (2017).
[29] H. Takenaka, I. Grinberg, and A. M. Rappe, Nat. Mater. **17**, 657 (2018).
[30] J. Kim, H. Takenaka, Y. Qi, A. R. Damodaran, A. Fernandez, R. Gao, M. R. McCarter, S. Saremi, L. Chung, A. M. Rappe *et al.*, Adv. Mater. **31**, 1901060 (2019).
[31] I. Brown and R. Shannon, Acta Crystallogr., Sect. A **29**, 266 (1973).
[32] I. Brown and K. K. Wu, Acta Crystallogr., Sect. B **32**, 1957 (1976).
[33] Y.-H. Shin, J.-Y. Son, B.-J. Lee, I. Grinberg, and A. M. Rappe, J. Phys.: Condens. Matter **20**, 015224 (2008).
[34] I. D. Brown, Chem. Rev. **109**, 6858 (2009).
[35] D. G. Pettifor, I. I. Oleinik, D. Nguyen-Manh, and V. Vitek, Comput. Mater. Sci. **23**, 33 (2002).
[36] M. Finnis and J. Sinclair, Philos. Mag. A **50**, 45 (1984).
[37] M. A. Harvey, S. Baggio, and R. Baggio, Acta Crystallogr., Sect. B **62**, 1038 (2006).
[38] Y.-H. Shin, I. Grinberg, I.-W. Chen, and A. M. Rappe, Nature (London) **449**, 881 (2007).
[39] S. Liu, I. Grinberg, and A. M. Rappe, Nature (London) **534**, 360 (2016).
[40] H. Lu, S. Liu, Z. Ye, S. Yasui, H. Funakubo, A. M. Rappe, and A. Gruverman, Appl. Phys. Lett. **110**, 222903 (2017).
[41] F. Chen, J. Goodfellow, S. Liu, I. Grinberg, M. C. Hoffmann, A. R. Damodaran, Y. Zhu, P. Zalden, X. Zhang, I. Takeuchi, A. M. Rappe, L. W. Martin, H. Wen, and A. M. Lindenberg, Adv. Mater. **27**, 6371 (2015).
[42] P. Agrawal, M. Campanini, A. Rappe, S. Liu, V. Grillo, C. Hébert, R. Erni, D. Passerone, and M. D. Rossell, Phys. Rev. Mater. **3**, 034410 (2019).
[43] P. Hohenberg and W. Kohn, Phys. Rev. **136**, B864 (1964).
[44] W. Kohn and L. J. Sham, Phys. Rev. **140**, A1133 (1965).
[45] See Supplemental Material at http://link.aps.org/supplemental/10.1103/PhysRevB.100.174109 for further details about the parametrization of the interatomic potential, the simulation cell size dependence of the polarization vs temperature curves, the ability of the interatomic potential to reproduce the elastic properties of pure $BaTi_3$ and $SrTiO_3$, and the changes in the order of the phase transitions of $Ba_xSr_{1-x}TiO_3$.

[46] F. Chen, Y. Zhu, S. Liu, Y. Qi, H. Y. Hwang, N. C. Brandt, J. Lu, F. Quirin, H. Enquist, P. Zalden, T. Hu, J. Goodfellow, M. J. Sher, M. C. Hoffmann, D. Zhu, H. Lemke, J. Glownia, M. Chollet, A. R. Damodaran, J. Park, Z. Cai, I. W. Jung, M. J. Highland, D. A. Walko, J. W. Freeland, P. G. Evans, A. Vailionis, J. Larsson, K. A. Nelson, A. M. Rappe, K. Sokolowski-Tinten, L. W. Martin, H. Wen, and A. M. Lindenberg, Phys. Rev. B **94**, 180104(R) (2016).

[47] Y. Qi, S. Liu, A. M. Lindenberg, and A. M. Rappe, Phys. Rev. Lett. **120**, 055901 (2018).

[48] A. R. Damodaran, S. Pandya, Y. Qi, S.-L. Hsu, S. Liu, C. Nelson, A. Dasgupta, P. Ercius, C. Ophus, L. R. Dedon *et al.*, Nat. Commun. **8**, 14961 (2017).

[49] P. Giannozzi, S. Baroni, N. Bonini, M. Calandra, R. Car, C. Cavazzoni, D. Ceresoli, G. L. Chiarotti, M. Cococcioni, I. Dabo, A. D. Corso, S. de Gironcoli, S. Fabris, G. Fratesi, R. Gebauer, U. Gerstmann, C. Gougoussis, A. Kokalj, M. Lazzeri, L. Martin-Samos, N. Marzari, F. Mauri, R. Mazzarello, S. Paolini, A. Pasquarello, L. Paulatto, C. Sbraccia, S. Scandolo, G. Sclauzero, A. P. Seitsonen, A. Smogunov, P. Umari, and R. M. Wentzcovitch, J. Phys.: Condens. Matter **21**, 395502 (2009).

[50] N. J. Ramer and A. M. Rappe, Phys. Rev. B **59**, 12471 (1999).

[51] A. M. Rappe, K. M. Rabe, E. Kaxiras, and J. D. Joannopoulos, Phys. Rev. B **41**, 1227(R) (1990).

[52] J. P. Perdew, A. Ruzsinszky, G. I. Csonka, O. A. Vydrov, G. E. Scuseria, L. A. Constantin, X. Zhou, and K. Burke, Phys. Rev. Lett. **100**, 136406 (2008).

[53] S. Plimpton, J. Comput. Phys. **117**, 1 (1995).

[54] S. Nosé, J. Chem. Phys. **81**, 511 (1984).

[55] S. Nosé, Mol. Phys. **52**, 255 (1984).

[56] W. G. Hoover, Phys. Rev. A **31**, 1695 (1985).

[57] M. Parrinello and A. Rahman, Phys. Rev. Lett. **45**, 1196 (1980).

[58] M. Parrinello and A. Rahman, J. Appl. Phys. **52**, 7182 (1981).

[59] V. V. Lemanov, E. P. Smirnova, P. P. Syrnikov, and E. A. Tarakanov, Phys. Rev. B. **54**, 3151 (1996).

[60] C. Menoret, J. M. Kiat, B. Dkhil, M. Dunlop, H. Dammak, and O. Hernandez, Phys. Rev. B. **65**, 224104 (2002).

[61] M. Acosta, N. Novak, V. Rojas, S. Patel, R. Vaish, J. Koruza, G. Rossetti, Jr., and J. Rödel, Appl. Phys. Rev. **4**, 041305 (2017).

[62] S. Tinte, M. G. Stachiotti, S. R. Phillpot, M. Sepliarsky, D. Wolf, and R. L. Migoni, J. Phys.: Condens. Matter **16**, 3495 (2004).

[63] L. Walizer, S. Lisenkov, and L. Bellaiche, Phys. Rev. B **73**, 144105 (2006).

[64] T. Nishimatsu, A. Gruenebohm, U. V. Waghmare, and M. Kubo, J. Phys. Soc. Jpn. **85**, 114714 (2016).

[65] S. Tinte, M. G. Stachiotti, M. Sepliarsky, R. L. Migoni, and C. O. Rodriquez, J. Phys.: Condens. Matter **11**, 9679 (1999).

[66] W. Zhong, D. Vanderbilt, and K. M. Rabe, Phys. Rev. B **52**, 6301 (1995).

[67] G. Geneste, J. Phys.: Condens. Matter **23**, 125901 (2011).

[68] J. M. Vielma and G. Schneider, J. Appl. Phys. **114**, 174108 (2013).

[69] X. Li, T. Qiu, J. Zhang, E. Baldini, J. Lu, A. M. Rappe, and K. A. Nelson, Science **364**, 1079 (2019).

[70] P. Ghosez, X. Gonze, P. Lambin, and J.-P. Michenaud, Phys. Rev. B **51**, 6765 (1995).

[71] H. Unoki and T. Sakudo, J. Phys. Soc. Jpn. **23**, 546 (1967).

[72] R. Wahl, D. Vogtenhuber, and G. Kresse, Phys. Rev. B. **78**, 104116 (2008).

[73] L. Landau, Phys. Z. Sowjetunion **11**, 26 (1937).

[74] A. F. Devonshire, London, Edinburgh, Dublin Philos. Mag. J. Sci. **40**, 1040 (1949).

[75] V. Ginzburg and L. Landau, J. Exp. Theor. Phys. USSR **20**, 1064 (1950).

[76] S. Tinte, M. Stachiotti, M. Sepliarsky, R. Migoni, and C. Rodriguez, Ferroelectrics **237**, 41 (2000).

[77] K. Müller, Y. Luspin, J. Servoin, and F. Gervais, J. Phys. Lett. **43**, 537 (1982).

[78] P. Ghosez, D. Desquesnes, X. Gonze, and K. Rabe, in *Fundamental Physics of Ferroelectrics 2000: Aspen Center for Physics Winter Workshop*, AIP Conf. Proc. No. 535 (AIP, New York, 2000), pp. 102–110.

[79] H. Li, H. Zheng, L. Salamanca-Riba, R. Ramesh, I. Naumov, and K. Rabe, Appl. Phys. Lett. **81**, 4398 (2002).

[80] K. Johnston, X. Huang, J. B.Neaton, and K. M. Rabe, Phys. Rev. B. **71**, 100103(R) (2005).

[81] D. L. Kaiser, M. D. Vaudin, L. D. Rotter, J. E. Bonevich, I. Levin, J. T. Armstrong, A. L. Roytburd, and D. G. Schlom, J. Mater. Res. **14**, 4657 (1999).

[82] W. Tian, J. Jiang, X. Pan, J. Haeni, Y. Li, L. Chen, D. Schlom, J. Neaton, K. Rabe, and Q. Jia, Appl. Phys. Lett. **89**, 092905 (2006) .

[83] Y. Li, S. Y. Hu, D. Tenne, A. Soukiassian, D. Schlom, L. Chen, X. Xi, K. J. Choi, C. Eom, A. Saxena *et al.*, Appl. Phys. Lett. **91**, 252904 (2007).

[84] A. Bruchhausen, A. Fainstein, A. Soukiassian, D. G. Schlom, X. X. Xi, M. Bernhagen, P. Reiche, and R. Uecker, Phys. Rev. Lett. **101**, 197402 (2008).

[85] K. Kathan-Galipeau, P. Wu, Y. Li, L.-Q. Chen, A. Soukiassian, X. Xi, D. G. Schlom, and D. A. Bonnell, ACS Nano **5**, 640 (2010).

[86] A. Bruchhausen, A. Fainstein, S. Tinte, A. Soukiassian, D. Schlom, and X. Xi, Chin. J. Phys. **49**, 159 (2011).

[87] K. Kathan-Galipeau, P. Wu, Y. Li, L.-Q. Chen, A. Soukiassian, Y. Zhu, D. A. Muller, X. Xi, D. G. Schlom, and D. A. Bonnell, J. Appl. Phys. **112**, 052011 (2012).

[88] C.-H. Lee, N. D. Orloff, T. Birol, Y. Zhu, V. Goian, E. Rocas, R. Haislmaier, E. Vlahos, J. A. Mundy, L. F. Kourkoutis *et al.*, Nature (London) **502**, 532 (2013).

[89] G. Subramanyam, M. W. Cole, N. X. Sun, T. S. Kalkur, N. M. Sbrockey, G. S. Tompa, X. Guo, C. Chen, S. P. Alpay, G. A. Rossetti, Jr. *et al.*, J. Appl. Phys. **114**, 191301 (2013).

[90] V. Železný, A. Soukiassian, D. G. Schlom, and X. Xi, J. Appl. Phys. **115**, 184102 (2014).

[91] V. Železný, A. Soukiassian, X. Xi, and D. G. Schlom, Phase Transitions **87**, 929 (2014).

[92] P. Wu, X. Ma, Y. Li, C.-B. Eom, D. G. Schlom, V. Gopalan, and L.-Q. Chen, Appl. Phys. Lett. **107**, 122906 (2015).

[93] V. Železný, O. Caha, A. Soukiassian, D. G. Schlom, and X. X. Xi, Phys. Rev. B. **95**, 214110 (2017).

[94] X. Wei, A. L. Vasiliev, and N. P. Padture, J. Mater. Res. **20**, 2140 (2005).